Force-free swimming of a model helical flagellum in viscoelastic fluids

Bin Liu[a,1], Thomas R. Powers[a,b], and Kenneth S. Breuer[a]

[a]School of Engineering, Box D, Brown University, Providence, RI 02912; and [b]Department of Physics, Brown University, Providence, RI 02912

Edited by Harry L. Swinney, University of Texas at Austin, Austin, TX, and approved October 3, 2011 (received for review August 10, 2011)

We precisely measure the force-free swimming speed of a rotating helix in viscous and viscoelastic fluids. The fluids are highly viscous to replicate the low Reynolds number environment of microorganisms. The helix, a macroscopic scale model for the bacterial flagellar filament, is rigid and rotated at a constant rate while simultaneously translated along its axis. By adjusting the translation speed to make the net hydrodynamic force vanish, we measure the force-free swimming speed as a function of helix rotation rate, helix geometry, and fluid properties. We compare our measurements of the force-free swimming speed of a helix in a high-molecular weight silicone oil with predictions for the swimming speed in a Newtonian fluid, calculated using slender-body theories and a boundary-element method. The excellent agreement between theory and experiment in the Newtonian case verifies the high accuracy of our experiments. For the viscoelastic fluid, we use a polymer solution of polyisobutylene dissolved in polybutene. This solution is a Boger fluid, a viscoselastic fluid with a shear-rate-independent viscosity. The elasticity is dominated by a single relaxation time. When the relaxation time is short compared to the rotation period, the viscoelastic swimming speed is close to the viscous swimming speed. As the relaxation time increases, the viscoelastic swimming speed increases relative to the viscous speed, reaching a peak when the relaxation time is comparable to the rotation period. As the relaxation time is further increased, the viscoelastic swimming speed decreases and eventually falls below the viscous swimming speed.

motility | propulsion | rheology

Small motile organisms often swim in complex fluids. Mammalian spermatozoa beat their flagella to move through cervical fluid (1). The Lyme disease spirochete *Borrelia burgdorferi* flexes and rotates its body to move through the extracellular matrix of our skin (2). The nematode *Caenorhabditis elegans* undulates its body to move through soil saturated with water (3). While there is an extensive framework for understanding the mechanics of swimming of small organisms in purely viscous Newtonian liquids such as water, our understanding of the basic principles of swimming in non-Newtonian fluids is still in its infancy (4). The behavior of complex fluids is varied, and there are many possible non-Newtonian effects a swimmer could encounter, including elastic response of the fluid, shear-dependent viscosity, adhesion to suspended particles or fibers, or the permeability of a porous medium. In this article we focus on swimming in an elastic liquid, and our goal is to determine how the speed of a model bacterial swimmer is changed by elastic effects.

It is known that helically shaped bacteria such as *Leptospira* or *B. burgdorferi* swim more rapidly in solutions with methylcellulose than in nonviscoelastic solutions of the same viscosity (2, 5). On the other hand, *C. elegans*, which moves using planar undulations of its body, swims more slowly in a viscoelastic fluid than in a viscous fluid (6). Recent theoretical and computational work has also examined how elastic effects change swimming speed. The importance of elastic effects are quantified by the Deborah number De, defined as the ratio of the relaxation time τ of the fluid to the characteristic time scale of the swimmer. For an infinite sheet or filament deformed by low-amplitude traveling waves and suspended in a dilute polymer solution described by the Oldroyd-B model, the swimming speed is always less than the Newtonian speed and decreases with increasing Deborah number (7–9). These theoretical predictions agree roughly with the measurements of swimming *C. elegans* (6). Finite-length sheets with large-amplitude bending waves behave differently. If the propagating wave increases in amplitude from head to tail, then the swimmer moves faster in the viscoelastic solution than in the viscous solution until $\mathrm{De} \approx 1$; above this value, the ratio of the viscoelastic and viscous swimming speeds decreases and eventually falls below unity (10). Other theoretical work has shown that the speed of a swimmer in a viscous fluid with prescribed stroke can be enhanced by the addition of stationary obstacles (11) and can be either enhanced or slowed by the presence of a polymer network (12). *C. elegans* has also been observed to swim faster in a wet granular medium than in water, an effect that has been attributed to an enhancement of the asymmetry of the drag of slender objects in wet granular media (3). To summarize, both theory and experiments indicate that whether or not a swimmer with a prescribed stroke moves faster or slower in a complex fluid depends sensitively on the geometry of the swimming stroke and the rheology of the complex fluid. The theoretical work considers highly idealized models, whereas the experimental work has thus far used real biological swimmers with all their inherent complexity and variability. However, there are very few highly controlled model experiments that isolate the physics underlying swimming in a non-Newtonian fluid. To fill this gap, we report on precise, repeatable measurements using a model helical swimmer in a model viscoelastic fluid.

Our swimmer is a rotating rigid helix, plunged at constant speed V into a tank containing either a Newtonian fluid or a viscoelastic fluid (Fig. 1). The viscoelastic fluid is well approximated by a Boger fluid, a liquid with a shear-rate-independent viscosity (13, 14). The fluids are highly viscous to replicate the low Reynolds number environment of microorganisms. Zero-force swimming is achieved by adjusting the translation speed until the measured axial force is zero. Note that there is an external torque acting on the helix; this torque may be interpreted as the torque from the bacterial rotary motor, which is balanced by the counter-rotation of the cell body. We do not model the flow induced by the cell body. Our setup allows us to determine how swimming speed depends on helix rotation speed, helix geometry, and the material properties of the fluid. To verify the accuracy of our technique, we measure the motility of helices in silicone oil, which is Newtonian for the range of rotation speeds we study. Using slender-body theories and a boundary-element method, we precisely calculate the ratio of swimming speed to rotation speed and find excellent agreement between theory and experiment. This part of our work is closely related to Hancock's calculations of the

Author contributions: B.L., T.R.P., and K.S.B. designed research; B.L., T.R.P., and K.S.B. performed research; and B.L., T.R.P., and K.S.B. wrote the paper.

The authors declare no conflict of interest.

This article is a PNAS Direct Submission.

[1]To whom correspondence should be addressed. E-mail: bin_liu@brown.edu.

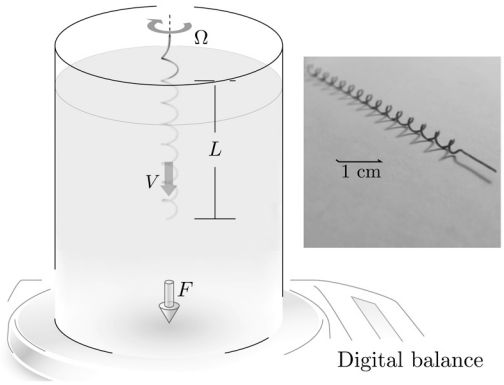

Fig. 1. Setup for measuring the motility of a rotating helix. The helix rotates about the vertical direction with rotation rate Ω. A linear stage (not shown for clarity) slowly inserts the helix into a viscous or viscoelastic fluid with a speed V. The net hydrodynamic force on the helix is determined by a sensitive laboratory balance beneath the tank. (*Inset*) A typical helix used in our experiment.

swimming speeds of filaments supporting propagating helical waves, which he compared to Taylor's experiments (15).

Results

Of the many possible non-Newtonian effects, we focus on viscoelasticity, in which the fluid has a fading memory characterized by a relaxation time τ. To minimize other non-Newtonian effects, we use a standard Boger fluid, a dilute solution of polyisobutylene (PIB) in polybutene (PB) (13, 14). We use two different concentrations. As shown in Fig. 2*A*, the viscosity η of each concentration of the polymer solution is nearly constant, decreasing by only 10% over a range where the shear rate $\dot{\gamma}$ varies by three orders of magnitude. In the shear-rate regime typical for our experiments, 0.1–100 rad/s, the viscosity $\eta = 40.5 \pm 0.2$ Pa · s for $c = 3{,}000$ ppm, and $\eta = 49.4 \pm 1.2$ Pa · s for $c = 6{,}000$ ppm. Although a perfect Boger fluid should have a shear-rate independent viscosity, the modest decrease that we observe can be captured using a nonlinear viscoelastic model which allows for polymer interactions (16). A very small value of the nonlinear interaction parameter ($a = 0.02$) was found to be necessary to match the observed decrease in viscosity η.

A typical Boger fluid consists of multiple elastic modes associated with different relaxation times. Its linear viscoelasticity subject to low-amplitude oscillation at frequency ω can thus be expressed as (17)

$$G'(\omega) = \sum_{i=1}^{N} g_i \tau_i^2 \omega^2 / (1 + \omega^2 \tau_i^2), \qquad [1]$$

$$G''(\omega) = \omega \eta_s + \sum_{i=1}^{N} g_i \tau_i \omega / (1 + \omega^2 \tau_i^2), \qquad [2]$$

where $G'(\omega)$ and $G''(\omega)$ are the storage modulus and loss modulus, respectively; η_s is the viscosity of the Newtonian solvent and g_i are the fitting parameters for each relaxation time τ_i. The dynamic moduli (G' and G'') and the spectra of relaxation times τ_i were determined from unsteady rheometry experiments, and the fitting parameters g_i were obtained by fitting the Oldroyd-B equations Eq. **1** and **2** following the method used by Baumgaertel and Winter (17). Four well-defined discrete relaxation times were found from the rheometry spectra ($\tau_i = 0.005, 0.13, 0.50$, and 2.13 sec.) and result in an excellent fit to the measured storage and loss moduli (Fig. 2*B*, solid lines). The relaxation times were the same for both PIB concentrations.

By computing an average relaxation time $\langle \tau \rangle$, using the effective viscosity of each mode $g_i \tau_i$ as the weight:

$$\langle \tau \rangle = \sum_{i=1}^{N} g_i \tau_i^2 / \sum_{i=1}^{N} g_i \tau_i, \qquad [3]$$

a simpler Oldroyd-B model was also fit to the data (Fig. 2*B*, dashed lines, $\langle \tau \rangle = 0.61$ s for $c = 3{,}000$ ppm and 0.58 s for $c = 6{,}000$ ppm). Both the single and multiple-relaxation time models show excellent agreement with the measurements and exhibit the expected theoretical behavior at low angular frequencies (18). The predicted behavior of the storage modulus G' obtained using a single relaxation time model does not, however, capture the measured behavior at higher frequencies with complete fidelity. As expected for a dilute solution, the average ratio of the storage moduli for concentrations $c = 6{,}000$ ppm and $c = 3{,}000$ ppm is 2.19 ± 0.25 for the range of frequencies tested.

To measure the force exerted on the helix by the fluid, the tank is placed on a sensitive balance, and the helix is rotated at rotation rate Ω as it plunges into the fluid with speed V, which can be as large as 2 mm/s. As the helix translates, the force F, is recorded as a function of the immersed length, L (Fig. 1). The total force is composed of both a hydrodynamic force, $F_{\text{hydro}}(L,\Omega,V)$, due to thrust, and a static force, $F_{\text{static}}(L)$ due to buoyancy and capillary effects at the liquid-air interface. $F_{\text{static}}(L)$ can be determined in a calibration measurement, after which F_{hydro} is determined for each L by subtracting F_{static} from the measured total force. Note that because the helix is inserted from above, a positive vertical force on the helix represents a drag, and a negative vertical force on the helix is a thrust. For each trial, we measure F_{hydro} as the helix is driven into the fluid. Fig. 3 shows that for small speeds V, the hydrodynamic force on the helix is negative, corresponding to thrust. At higher speeds, the hydrodynamic force on the helix is positive, corresponding to drag.

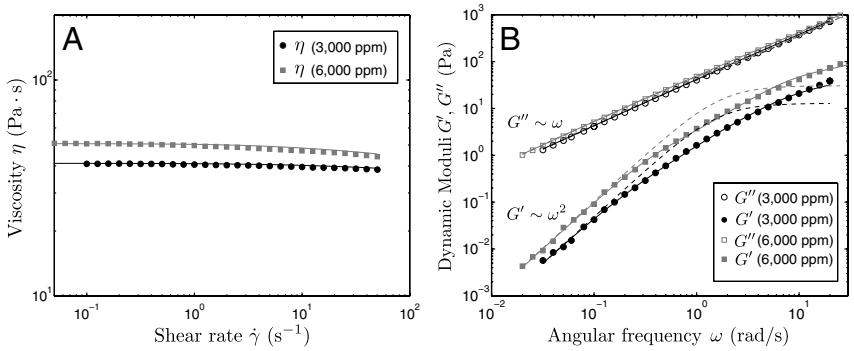

Fig. 2. Rheological properties of a solution of polyisobutylene (PIB) in polybutene (PB) for concentrations $c = 3{,}000$ ppm and 6,000 ppm. (*A*) Viscosity vs. shear rate. The symbols represent experimental measurements while the solid line is the fit to the data using a nonlinear viscoelastic model (16). (*B*) Storage modulus G' (filled symbols) and loss modulus G'' (open symbols) vs. oscillating frequency ω. The dotted lines show the fit to the data using an Oldroyd-B model with a single relaxation time, while the solid lines show the fit to the measurements obtained using four relaxation times (17). The elastic component of the fluid, as characterized by G', increases as the concentration of PIB increases.

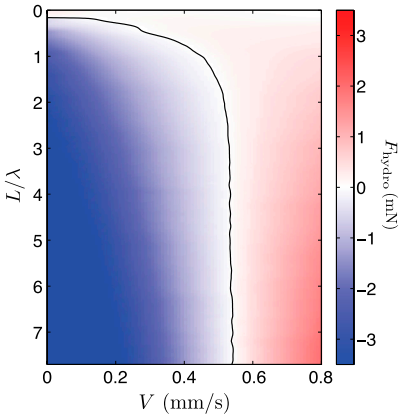

Fig. 3. Colormap of hydrodynamic force F_{hydro} on a helix as a function of the immersed depth L and speed V as it is inserted in a viscoelastic fluid (a solution of PIB in PB with $c = 6{,}000$ ppm) at a fixed rotation rate $\Omega = 2.093$ rad/s. The helix has radius $R = 1.54$ mm and pitch $\lambda = 5.68$ mm. As the speed V of the helix increases, the hydrodynamic force changes from thrust (blue, along the direction of insertion) to drag (red, against the insertion). The black line is the $F_{\mathrm{hydro}} = 0$ contour, corresponding to the condition of force-free swimming. The colormap for the viscous case is similar.

Through linear interpolation, F_{hydro} can be expressed as a function of V and L (Fig. 3).

The contour line with $F_{\mathrm{hydro}} = 0$ (black line in Fig. 3) shows the speed V_0 required for force-free swimming as a function of L. We use V_0 to denote the free-swimming speed for the Newtonian liquid and V_p to denote the free-swimming speed for the polymer solution. Note that V_0 is independent of the immersed length L of the helix once L is greater than roughly one pitch length, $L \gtrsim \lambda$. In the polymer solution, the free-swimming speed V_p becomes independent of immersed length once $L \gtrsim \lambda$ as well. Therefore, we conclude that end effects are negligible once a pitch length has been immersed. Fig. 4 shows how the hydrodynamic force per length depends on time or, equivalently, immersed length, for several different rotation speeds. It is difficult to untangle the relative importance of the relaxation of stress from the influence of end effects when the immersed length is small (i.e., at early times). However, comparison of the force per length vs. time for the Newtonian and viscoelastic cases (Fig. 4, *Inset*) shows that the viscoelastic force decays more slowly than the viscous force. Note that because the relaxation times of the viscoelastic fluids tested (< 1 s) are much less than the transit times for each helix tested (> 20 s) we can safely assume that transient viscoelastic effects have relaxed once the steady-state force is achieved.

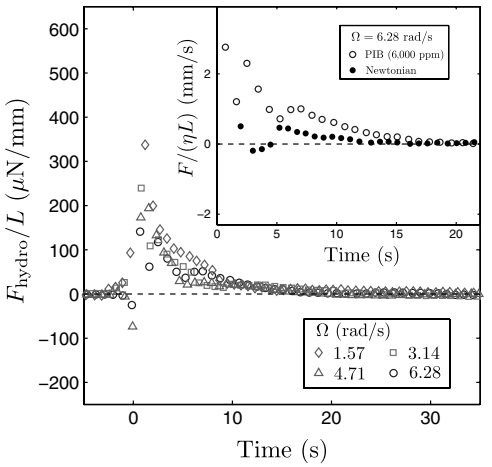

Fig. 4. Time dependence of the hydrodynamic force F_{hydro} acting on a helix rotating with rate Ω and inserted into a viscoelastic liquid at the associated free-swimming speed V_p. The liquid is 6,000 ppm PIB in PB, with a relaxation time $\tau = 0.58$ s. The helix first touches the air–liquid interface at $t = 0$. The initial dependence of force on time (or equivalently, immersed length) is a finite-length effect, folded together with the relaxation of stress arising from viscoelasticity. The inset shows a comparison to the Newtonian case.

Fig. 5 shows the force-free swimming velocity as a function of rotation rate Ω. As expected, V_0 increases linearly with Ω for the Newtonian fluid (19–21). The slope of the V_0 vs. Ω curve is constant to within 1%. Fig. 5 also reveals that the effect of viscoelasticity is to enhance the swimming speed V_p relative to the Newtonian speed. The enhancement is small, but it systematically increases with polymer concentration.

Before describing how the enhancement depends on Deborah number, we pause to assess the accuracy of our measurement technique by comparing the measurements of the swimming speed in the Newtonian liquid with predictions from theory. The simple geometry of a helix allows detailed comparison between measurement and theory. For the Newtonian liquid, the linear dependence of V_0 on Ω means that $V_0/(\Omega R)$ is an invariant for a helix of given pitch angle θ and aspect ratio d/l, where d is filament diameter and l is the contour length per helical pitch. Fig. 6 shows measurements of the ratio $V_0/(\Omega R)$ for helices with various θ and d/l. Because our purpose is to assess the accuracy of our measurements, we only report the results of the theory; the details of the calculations will be treated in a different publication. Because the helix is long and thin, we may approximate it by a one-dimensional distribution of singular solutions to Stokes equations. This approximation is the basis for slender-body theory (SBT) (22–26). There are various versions of SBT; in Fig. 6 we show the results for two commonly used approaches, Lighthill's SBT and Johnson's SBT. Because these theories approximate the filament as a one-dimensional distribution of singular solutions, they always have an error, which can be as small as d/L for Lighthill's SBT (25) and as small as $(d/L)^2 \log(d/L)$ for Johnson's SBT (26). Nevertheless, Fig. 6 shows that both versions of SBT agree extremely well with the measurements. We also used a boundary-element technique to calculate $V_0/(\Omega R)$ for the helix in the viscous liquid. In this method, singular solutions are distributed over the two-dimensional surface of the helix. The increased resolution comes with a cost of increased computing time, but unlike SBT, there is no intrinsic error for the boundary-element method. We can reduce the computational time somewhat by exploiting the fact that end effects are negligible

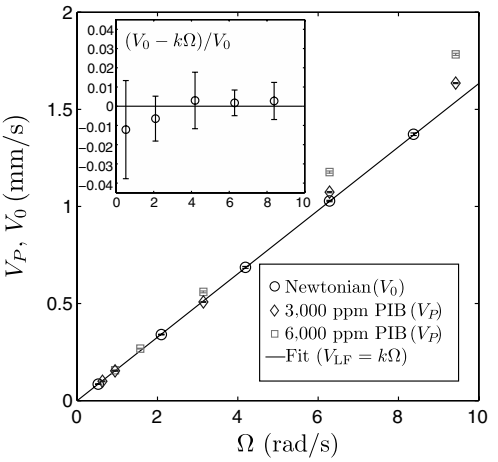

Fig. 5. Free-swimming speed of a rotating helix vs. rotation rate for Newtonian and non-Newtonian fluids. The helix has $\lambda = 4.29$ mm, $R = 1.54$ mm, and $d = 0.6$ mm. The straight line is a linear fit to the measurements for the Newtonian fluid and the enhancement of swimming speed in PIB is clearly observed. The inset shows the deviation from linearity for the Newtonian fluid as a function of rotational speed.

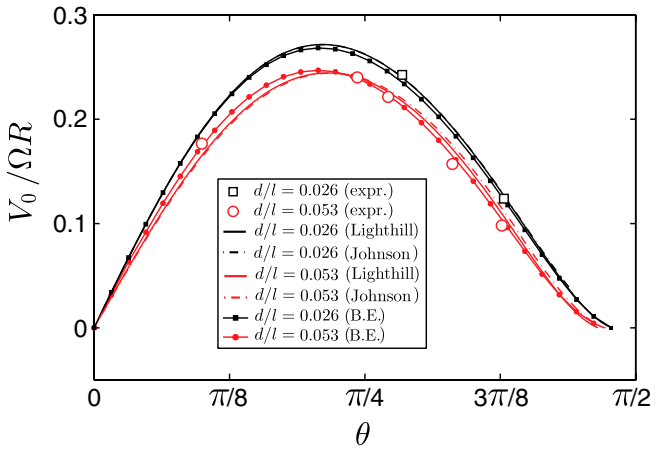

Fig. 6. The normalized swimming speed $V_0/\Omega R$ of helices of various pitch angles θ and two different aspect ratios d/l in a viscous fluid. The graph shows experimental measurements (open circles and squares), the predictions of Lighthill's and Johnson's slender-body theories, and a boundary-element method (B.E.).

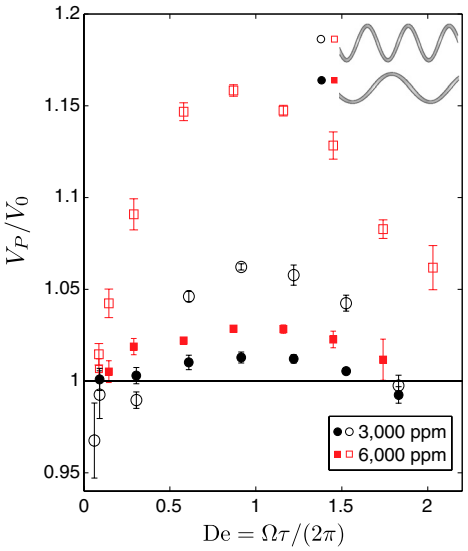

Fig. 7. Ratio of free-swimming speed in the viscoelastic fluid V_p to that in the Newtonian fluid V_0, as a function of the Deborah number De, for two different polymer solutions and two different helices.

and by using the symmetry of an infinite helix to simplify the calculation. The agreement between the predictions of the boundary-element method and the measurements is excellent (Fig. 6). The agreement between experiment and theory also confirms that the experimental configuration can be safely assumed to represent the steady motion of an unbounded helix in an infinite domain and that the effects of the container walls are negligible.

With the experimental technique quantitatively validated using the Newtonian fluid, we return to the study of the helix in the polymer fluid. Fig. 7 shows the measurements of the force-free swimming speeds V_p of helices in polymeric solutions of two different elasticities. We measure the rotation frequency $\Omega/(2\pi)$ in units of the relaxation time using the Deborah number, $\mathrm{De} = \Omega\tau/(2\pi)$. Note that our definition of the Deborah number is the same as that of ref. 10 and differs by that of refs. 7–9 by a factor of 2π. For a given helical geometry, V_p/V_0 is nearly unity at small De, which is expected because the fluid becomes less elastic as the rate of deformation decreases. Note that at the smallest value of De for which we take measurements, the hydrodynamic forces are smallest and experimental error, primarily due to a small amount of fluid retained on the withdrawn helix from previous trials, is relatively higher compared to measurements at higher De. We should emphasize that for each point plotted in Fig. 7, approximately five experiments are needed, in which the translation speed V is changed, in order to determine the zero-force swimming speed for those conditions. The aggregate data, though compactly presented, thus represents hundreds of hours of carefully controlled data acquisition.

As De increases, the ratio V_p/V_0 becomes greater than unity, showing an enhancement of the free-swimming speed in the viscoelastic fluid relative to the Newtonian reference. The enhancement peaks at $\mathrm{De} \sim 1$, where the rotation rate Ω matches the relaxation rate τ of the viscoelastic fluid. The enhancement is sensitive to the helical geometry. The helix with $\theta = 0.38\pi$ (upper helix, Fig. 7) has a maximum enhancement that is nearly five times that of the helix with $\theta = 0.27\pi$ (lower helix, Fig. 7). The enhancement also depends on the elasticity of the liquid. As the concentration of PIB doubles and $G = \eta - \eta_s/\tau$ increases from 10.5 Pa to 26.4 Pa, the maximum enhancement increases by a factor between two and three. As De increases beyond unity, V_p/V_0 decreases and the helix eventually swims more slowly than V_0. We did not make measurements for $\mathrm{De} > 2$, since at those high rotation rates the transit time for the helix is no longer large compared to the relaxation time.

Discussion

The most striking feature of this study is the enhancement of swimming speed of a rotating helix in a viscoelastic fluid near $\mathrm{De} = 1$, in contrast with the decrease observed in the swimming speed of nematodes using planar undulations in a Boger fluid (6). Thus, the nature of the dependence of swimming speed on De appears to depend strongly on the geometry of the waveform used for swimming. This conclusion is further supported by the sensitivity of the peak enhancement of swimming speed on the pitch angle of the helix (Fig. 7). The enhancement near $\mathrm{De} = 1$ is reminiscent of the simulated behavior of a large-amplitude finite-length swimmer in two dimensions (10). In that simulation and in our experiment, the peak enhancement of swimming speed occurs when the time scale for the strained fluid to relax matches that of the periodic forcing. Note, however, that in the case of the large-amplitude swimmer (10), the stress at the end of the swimmer played an important role, whereas in our experiment we do not expect end effects to underly the enhancement of swimming speed because we saw that end effects are negligible once the immersed length is longer than one wavelength.

Two concerns with our experiment are the possibility of a systematic error and whether we can ascribe with certainty elastic effects as the source of the swimming speed enhancement. The simplicity of the method, and the accuracy with which we reproduce the theoretical predictions for swimming in a Newtonian fluid (Fig. 6), helps to build confidence in the validity of the measurements. Similarly, although the test fluid is not a perfect Boger fluid, the changes in viscosity are extremely small, particularly over the range of low shear rates that characterize our experiments. Furthermore, the very modest shear thinning is monotonic while the swimming speed enhancement exhibits a clear maximum. Likewise, the elastic behavior of the PIB is as one would expect: the storage and loss moduli, G' and G'', are well modeled by the ideal asymptotic behavior ($G' \propto \omega^2$, $G'' \propto \omega$) at the lower frequencies characteristic of the experiments. There is, to be sure, evidence of nondilute effects in the fluid behavior. The storage and loss moduli and the moderate decreasing viscosity (Fig. 2) do fit a nondilute theory (16), and as noted above, the modulus G increases by a factor of 2.51 despite the fact that the concentration only increases by a factor of 2. Nevertheless, despite the fact that the fluid is not an ideal Oldroyd-B fluid, it is well approximated by that model, which indicates that the observed peak in swimming speed is due to the elasticity of the fluid. Detailed nu-

merical simulations using both the dilute single-relaxation model and the nondilute multiple-relaxation models can test these assertions, and velocimetry measurements (currently underway) will provide further insight regarding the similarities and differences between the current configuration and other planar and undulatory propulsive mechanisms.

We expect that the experimental approach will be useful for other situations. For example, it has recently been shown that the small but nonzero sedimentation force on a swimming *Volvox carteri* has a profound effect on the flow, with the Stokeslet component dominating the flow near the organism (27). This effect could be studied using our technique. Likewise, although our experiment is performed at low Reynolds number, the method is not limited to cases where the inertia of the fluid is negligible. As long as there is sufficient time to immerse the entire helix, a steady terminal speed will be achieved, even at high Reynolds number. However, maintaining a separation between the immersion time and the fluid relaxation time remains critical and might prove challenging at higher swimming speeds.

Finally, our experiment suggests new directions for modeling swimming microorganisms in viscoelastic fluids. There are several natural directions for further study. The discrepancy between the experiment and the predictions for the swimming speed of a filament supporting small-amplitude helical traveling waves (8) suggests that unlike the Newtonian case, rigidly rotating helices and filaments with propagating helical waves behave differently in a viscoelastic medium. Because the discrepancy emerges at small Deborah number, it would be useful to make an expansion about the Newtonian case for small De, as has been done for spheres falling near a wall in a weakly viscoelastic fluid (28). Alternatively, insight may be gained by applying the three-dimensional flow theorem of Giesekus, which states that for special choices of the coefficients in the constitutive relation for a viscoelastic fluid, the flow field is the same as that of a Newtonian fluid at zero Reynolds number, and the pressure may be calculated from this flow (29). It is not expected that these analytic approaches will be able to capture the maximum in $V_P/(\Omega R)$ for finite De; numerical approaches, such as were used in ref. 10, will be required for this task.

Materials and Methods

The Newtonian fluid is a high molecular weight silicone oil (Dow-Corning DC-200) with viscosity $\eta \approx 100$ Pa · s and density $\rho \approx 900$ kg/m^3. The Boger fluid is prepared with a dilute solution of polyisobutylene (PIB) in a polybutene (PB) solvent (both, Sigma Aldrich). The PIB and PB have average molecular weights of 420 kDa and 920 Da, respectively. The solvent PB is Newtonian, with viscosity $\eta_s = 34.1 \pm 0.1$ Pa · s at room temperature (20 °C). To thoroughly mix the PIB with the highly viscous solvent, we follow the recipe used by Vermant et al. (30), where 2-chloropropane is used as an intermediate fluid to dissolve the PIB. The 2-chloropropane is then removed from the mixture using a vacuum rotary evaporator. Two different concentrations of the dissolved polymers, $c = 3{,}000$ ppm and $c = 6{,}000$ ppm were prepared. The rheological properties of all the fluids used in the study were measured using a TA Instruments AR 2000 Rheometer.

The model flagella are helices with radius $R \approx 1$ mm, approximately 10 cm long, formed from a piece of thin zinc-galvanized steel wire, with a round cross-section of diameter $d = 0.6$ mm or $d = 0.3$ mm. One end of the helical wire is straight and axially aligned to easily attach to a servo motor operated at a constant speed, $\Omega \lesssim 10$ rad/s. The motor sits on a motorized linear stage that translates with velocity, $V < 2$ mm/s, along the axial direction of the helix. The Reynolds number $\mathrm{Re} = \rho\Omega R^2/\eta$ is never greater than 10^{-2}, which ensures that inertial effects remain negligible. To avoid wall effects (31), the diameter of the tank is at least 20 times greater than the radius of the helix, which is centered in the tank. The tank sits on a top-loading analytical balance (Setra SI-410S), with a sensitivity of ≈ 10 μN, which is used to measure the propulsive force. Note that when the helix is rotated in the Boger fluid, the rod-climbing effect (29) does not contribute an additional component to the thrust because the surface deformation is a response to the normal stress imbalance created by the fluid rotation.

ACKNOWLEDGMENTS. We thank Jinkee Lee and Anubhav Tripathi for the use of their rheometer; Chongyoup Kim for advice on the preparation of the viscoelastic fluid; and Eric Keaveny, Gareth McKinley, and Hepeng Zhang for useful discussions. T.R.P. is grateful to Roman Stocker and the Environmental Microfluidics Group at MIT for hospitality while some of this work was completed. This work was supported in part by National Science Foundation Grants CBET-0854108 (T.R.P. and K.S.B.) and CTS-0828239 (K.S.B.).

1. Suarez SS, Pacey AA (2006) Sperm transport in the female reproductive tract. *Human Reprod Update* 12:23–37.
2. Kimsey RB, Spielman A (1990) Motility of the Lyme disease spirochetes in fluids as viscous as the extracellular matrix. *J Infect Dis* 162:1205–1208.
3. Jung S (2010) Caenorhabditis elegans swimming in a saturated particulate system. *Phys Fluids (1994)* 22:031903.
4. Lauga E, Powers TR (2009) The hydrodynamics of swimming microorganisms. *Rep Prog Phys* 72:096601.
5. Berg HC, Turner L (1979) Movement of microorganisms in viscous environments. *Nature* 278:349–351.
6. Shen XN, Arratia PE (2011) Undulatory swimming in viscoelastic fluids. *Phys Rev Lett* 106:208101.
7. Lauga E (2007) Propulsion in a viscoelastic fluid. *Phys Fluids (1994)* 19:083104.
8. Fu HC, Powers TR, Wolgemuth CW (2007) Theory of swimming filaments in viscoelastic media. *Phys Rev Lett* 99:258101.
9. Fu HC, Wolgemuth CW, Powers TR (2009) Swimming speeds of filaments in nonlinearly viscoelastic fluids. *Phys Fluids (1994)* 21:033102.
10. Teran J, Fauci L, Shelley M (2010) Viscoelastic fluid response can increase the speed and efficiency of a free swimmer. *Phys Rev Lett* 104:038101.
11. Leshansky AM (2009) Enhanced low-Reynolds-number propulsion in heterogeneous viscous environments. *Phys Rev E Stat Nonlin Soft Matter Phys* 80:051911.
12. Fu HC, Shenoy VB, Powers TR (2010) Low reynolds number swimming in gels. *EPL* 91:24002 arXiv:1004.1339.
13. Boger DV (1977) A highly elastic constant-viscosity fluid. *J Nonnewton Fluid Mech* 3:87–91.
14. James DF (2009) Boger fluids. *Annu Rev Fluid Mech* 41:129–142.
15. Hancock GJ (1953) The self-propulsion of microscopic organisms through liquids. *Proc R Soc Lond A Math Phys Sci* 217:96–121.
16. Acierno D, FP la Mantia GM, Titomanlio G (1976) A non-linear viscoelastic model with structure-dependent relaxation times: I. basic formulation. *J Nonnewton Fluid Mech* 1:125–146.
17. Baumgaertel M, Winter HH (1989) Determination of discrete relaxation and retardation time spectra from dynamic mechanical data. *Rheol Acta* 28:511–519.
18. Larson RG (1998) The Structure and Rheology of Complex Fluids. (Oxford Univ Press, New York).
19. Purcell EM (1977) Life at low Reynolds-number. *Am J Phys* 45:3–11.
20. Purcell EM (1997) The efficiency of propulsion by a rotating flagellum. *Proc Natl Acad Sci USA* 94:11307–11311.
21. Chattopadhyay S, Moldovan R, Yeung C, Wu XL (2006) Swimming efficiency of bacterium escherichia coli. *Proc Natl Acad Sci USA* 103:13712–13717.
22. Gray J, Hancock GJ (1955) The propulsion of sea-urchin spermatozoa. *J Exp Biol* 32:802–814.
23. Lighthill J (1976) Flagellar hydrodynamics—neumann, jv lecture, 1975. *SIAM Rev* 18:161–230.
24. Lighthill J (1996) Helical distribution of stokeslets. *J Eng Math* 30:35–78.
25. Lighthill J (1996) Reinterpreting the basic theorem of flagellar hydrodynamics. *J Eng Math* 30:25–34.
26. Johnson R (1980) An improved slender-body theory for stokes-flow. *J Fluid Mech* 99:411–431.
27. Drescher K, Goldstein R, Michel N, Polin M, Tuval I (2010) Direct measurement of the flow field around swimming microorganisms. *Phys Rev Lett* 105:168101.
28. Becker LE, McKinley GH, Stone HA (1996) Sedimentaion of a sphere near a plane wall: Weak non-Newtonian and inertial effects. *J Nonnewton Fluid Mech* 63:201–233.
29. Bird RB, Armstrong RC, Hassager O (1987) *Dynamics of Polymeric Liquids, Fluid Mechanics*, (Wiley, New York), Vol. 1.
30. Vermant J, Cioccolo G, Nair K, Moldenaers P (2004) Coalescence suppression in model immiscible polymer blends by nano-sized colloidal particles. *Rheol Acta* 43:529–538.
31. Fidleris V, Whitmore RL (1961) Experimental determination of the wall effect for spheres falling axially in cylindrical vessels. *Brit J Appl Phys* 12:490–494.